

Interactive Occlusion Boundary Estimation through Exploitation of Synthetic Data

Lintao XU, Chaohui WANG

LIGM, Univ Gustave Eiffel, École des Ponts, CNRS, France

Abstract

Occlusion boundaries (OBs) geometrically localize the occlusion events in a 2D image, and contain useful information for addressing various scene understanding problems. To advance their study, we have led the investigation in the following three aspects. Firstly, we have studied interactive estimation of OBs, which is the first in the literature, and proposed an efficient deep-network-based method using multiple-scribble intervention, named DNMMSI, which significantly improves the performance over the state-of-the-art fully-automatic methods. Secondly, we propose to exploit the synthetic benchmark for the training process, thanks to the particularity that OBs are determined geometrically and unambiguously from the 3D scene. To this end, we have developed an efficient tool, named Mesh2OB, for the automatic generation of 2D images together with their ground-truth OBs, using which we have constructed a synthetic benchmark, named OB-FUTURE. Abundant experimental results demonstrate that leveraging such a synthetic benchmark for training achieves promising performance, even without the use of domain adaptation techniques. Finally, to achieve a more compelling and robust evaluation in OB-related research, we have created a real benchmark, named OB-LabName¹, consisting of 120 high-resolution images together with their ground-truth OBs, with precision surpassing that of previous benchmarks. We will release DNMMSI with pre-trained parameters, Mesh2OB, OB-FUTURE, and OB-LabName to support further research.

1. Introduction

Occlusion is a common phenomenon in 2D images of natural scenes and poses a significant challenge to achieving high-quality visual understanding. Despite the numerous works on occlusion handling (e.g., [15, 24, 31, 48, 49, 65]), effectively addressing it remains a major challenge in computer vision. As a key feature for characterizing occlusions, *Occlusion Boundary* (OB) has been studied for a long time,

both independently (e.g., [3, 4, 16, 58, 62]) and in conjunction with orientations (i.e., occluder/occludee relationships) for OBs (e.g., [12, 48, 64, 65]). Various equivalents and analogues of it have been leveraged to improve the performance of scene understanding tasks, such as depth estimation, refinement, and ordering [14, 21, 43, 48, 70], as well as 3D reconstruction and mesh recovery [5, 22, 23, 28, 67].

A significant number of studies of OB estimation have been carried out (e.g., [12, 16, 17, 48, 58, 62]), mainly based on the benchmarks shown in Fig. 1(a-d). However, the Ground Truths (GTs) in those benchmarks² were subjectively labeled without any unified definition, making them open to debate. For instance, lots of objects' OBs in *Pascal instance occlusion dataset (PIOD)* are overlooked, and only visible depth discontinuities in *NYUv2-OC++* are annotated, which results in incomplete object contours. The presence of subjective bias in their provided ground truths, along with the insufficient quality of the GTs (see Table 1), hinders the scientific and systematic study of OBs. To this end, a mathematical definition³ has been introduced in [62], which specifies that a small section of an OB represents an occlusion event caused by the 3D surfaces corresponding to the 2D regions on either side of the boundary, and that all occlusion events in the entire image are captured together. Based on this, OBs can be annotated impartially, as shown in Fig. 1(e, f). However, there is no previous benchmark where the GTs are based on this definition.

Three significant characteristics of the OB map that distinguish it from object contours in image segmentation (e.g., *ADE20K* [69]), amodal (instance) segmentation (e.g., *COCOA* [71]), and others are: non-closure, lack of semantic information, and consideration of self-occlusions (see more details in Section 3.1). These factors make OB estimation idiosyncratic and more challenging than segmentation-related problems in general, thereby increasing its significance and value as a subject of study.

All the above considerations have motivated our study of interactive OB estimation to enhance performance through human interaction and efficiently construct OB bench-

¹LabName will be specified upon acceptance.

²More details are included in the supplementary materials (SM).

³The definition is also included in the SM for easy reference.



Figure 1. Visualization of Occlusion Boundary Ground Truths (shown in red curves).

marks. To our knowledge, this is the first such study. Our main contributions are presented in three key aspects:

1. We predominantly propose a deep-learning-based scribble-based method for interactive OB estimation, named *DNMMSI*, leading to significant improvements of the performance over the state-of-the-art (SOTA) fully-automatic method *OPNet* [12] and 7 alternative interactive methods devised from interactive (object) segmentation methods [6, 7, 32–34, 36, 56]. Furthermore, *DNMMSI* shows promising potential in OB benchmark constructions through experiments.
2. Based on the fact that OB is geometrically defined without ambiguity [62], we propose to exploit the large amount of synthetic data to train the deep model for OB estimation. To this end, we introduce an efficient tool, named *Mesh2OB*, for automatically generating 2D images along with OBs, which has been utilized to establish a benchmark, named *OB-FUTURE*, comprising 19,186 synthetic samples sourced from the *3D-FUTURE* dataset [13]. Abundant experimental results demonstrate that leveraging such a synthetic benchmark for training achieves promising performance, even without the use of domain adaptation techniques. To the best of our knowledge, we are the first to generate OBs for 2D images directly from scene data. Our OB quality surpasses that of [48], which generates OB maps from depth and normal maps, demonstrating the superiority of directly exploring the 3D scene’s geometric information.
3. To achieve a more compelling and robust evaluation, we introduce a benchmark named *OB-LabName*, comprising two subsets: *OB-DIODE* and *OB-EntitySeg*. These subsets are constructed by meticulously labeling ground truths for 50 and 70 high-resolution images from two previous datasets [38, 60], significantly surpassing the precision of prior benchmarks (see Fig. 1).

2. Related Work

Fully-automatic OB Estimation remains a persistent challenge in Computer Vision, with numerous previous works addressing this issue. One subset of methods (e.g., [3, 11, 16, 19, 54, 57, 58, 62]) estimates OB maps from image sequences. Another subset of approaches (e.g., [12, 14, 17, 39, 48, 50–52, 59, 64, 65]) infers OB maps from 2D monocular images, either independently or along with the occluder/occludee relationships for OBs. For instance, [17] recovered occlusion boundaries using the traditional edge and region cues together with 3D surface and depth cues. [59] imposed a border ownership structure and simultaneously detected both boundaries and border ownership using structured random forests. [64] designed a one-stream deep method and a novel attention loss to tackle extreme boundary/non-boundary class imbalance. [50] utilized the displacement field to refine depth thus obtaining more accurate OBs. MTORL [12] proposed *OPNet* which only shares backbone features in the network and uses the side output to enhance the final OB prediction.

OB benchmarks include *CMU* [57], *BSDS ownership* [52], *PIOD* [65], *NYUv2-OC++* [50], and two synthetic datasets *iBims1_OR* and *InteriorNet_OR*, constructed by [48] using source data from [25, 30], with the GTs generated using the method of [48]. More details can be found in Table 1.

Interactive Segmentation (IS) aims to segment single objects (e.g., [56, 66]) or multiple objects (e.g., [27, 29]) by incorporating user interactions such as clicks (e.g., [34]), scribbles (e.g., [8]), and bounding boxes (e.g., [68]). It has also garnered significant attention in the field of medical image segmentation (e.g., [40, 63]). To date, the topic has seen significant advancements, along with the development of numerous deep learning-based methods (e.g., [7, 9, 18, 20, 34–36, 56, 66]). Scribble-based interactive segmentation typically places scribbles inside and/or out-

Table 1. **Comparison with Previous OB Benchmarks.** “syn” refers to synthetic, and † indicates that the data volume can scale with changes in the camera model. The image resolutions of *PIOD* and *OB-EntitySeg* are actually average values due to the varying image sizes.

Datasets	General Information				OB Characteristics			
	Data Volume	Image Resolution	Scene Type	GT Annotation	Full-image OB	Object-contour Completeness	Self-occlusion Boundary	Non-closure OB
<i>CMU</i> [57]	30	(640, 480)	real	manual	-	+	ignored	ignored
<i>BSDS Ownership</i> [52]	200	(481, 321)	real	manual	+	+	ignored	ignored
<i>PIOD</i> [65]	10,000	(475, 390)	real	manual	-	+	ignored	ignored
<i>NYUv2-OC++</i> [50]	654	(592, 440)	real	manual	-	-	incomplete	incomplete
<i>iBims1-OR</i> [48]	100	(640, 480)	real	syn	-	-	incomplete	incomplete
<i>InteriorNet-OR</i> [48]	10,000	(640, 480)	syn	syn	-	-	incomplete	incomplete
our <i>OB-FUTURE</i>	19,186†	(1080, 1080)	syn	syn	+	+	complete	complete
our <i>OB-DIODE</i>	50	(1024, 768)	real	manual	+	+	complete	complete
our <i>OB-EntitySeg</i>	70	(982, 882)	real(90%)	manual	+	+	complete	complete

side the object of interest, rather than on its boundaries. These scribbles act as corrective guides to refine prediction masks in error-prone areas [1, 2], or as general indicators to help models learn the complete object segmentation mask [8, 46]. Unfortunately, these scribble-based techniques require that object contours be fully closed, making them unsuitable for our problem. Several interactive segmentation methods [10, 26, 32, 41, 42] apply clicks on object contours for better performance, requiring much greater precision than the scribbles used in our approach.

The extension of IS to the full-image scenario is more relevant to our problem, yet it has been much less explored. Early works, such as [44, 45, 53, 61], laid the foundation for this topic. Later, with the resurgence of deep learning, a few works (e.g., [1, 2]) have also contributed to the development of deep-learning-based methods for this problem.

3. Method & Techniques

In this section, we successively present: preliminaries, our method *DNMMSI* for interactive OB estimation, and *Mesh2OB* for generating 2D images with OBs.

3.1. Preliminaries

Below are four distinctive characteristics of the OB map: (i) As depicted in Fig. 1 (e, f)⁴, occlusion boundaries are not always closed, due to the presence of self-occlusion phenomena; (ii) In OB estimation, all occlusion boundaries in the entire image need to be estimated, typically without incorporating semantic information or other study interest; (iii) A non-closed OB often partially or totally lies in a region with a single photometric model, as the two sides belong to the same object (e.g., the vanity unit in the bottom image of Fig. 1 (f)); and (iv) The OB map can be unambiguously and automatically derived from the 3D scene and camera settings, if they are given.

⁴More instances can be found in the supplementary materials.

3.2. Interactive Occlusion Boundary Estimation

In this problem, there are narrow, potentially open boundaries that need to be identified. After evaluating effectiveness, efficiency, and simplicity, we opted for scribble interaction. Here, a *scribble* is introduced, covering a broad region to provide the deep model with information on false positives (FPs) or false negatives (FNs) within that area. During the interaction stages, the user draws a set of FN-scribbles and FP-scribbles to highlight significant false negatives (FNs) and false positives (FPs). To integrate them into the model and refine its predictions, the FN-scribbles and FP-scribbles are encoded into a *FN interaction map* and a *FP interaction map*, respectively. These maps are binary images of the same size as the input image, with an intensity value of 1 for the regions covered by the corresponding scribbles. The combination of these maps is referred to as the *FN-FP map* hereafter (see examples in Fig. 4).

Overall Pipeline⁵ is illustrated in Fig. 2. Here are some explanations: (i) The input RGB image (3 channels), the FN-FP map (2 channels) and the previous output (1 channel) are stacked together and sent to the backbone and get the initial hierarchical features, then the features of different layers will be individually sent to the corresponding upsampling modules, before passing the OPMv2 modules, which are mainly composed of the strip convolution layers (see more details in the SM); (ii) In addition, the interaction path and the boundary path process the interaction maps and the RGB images separately; (iii) The decoder part aggregates all the features and outputs five OB probability maps, which are then fused together to achieve the final probability map; (iv) A non-maximum suppression (NMS) process is done on the probability map to obtain a thin edge map, which is commonly used in OB estimation [12, 48, 65]; (v) Finally, the *thresholding* process is applied to the probability map to obtain the final OB prediction. *DNMMSI* is modular with

⁵In Fig. 2, the FN-FP map and the previous output have been visually processed to provide a clearer illustration.

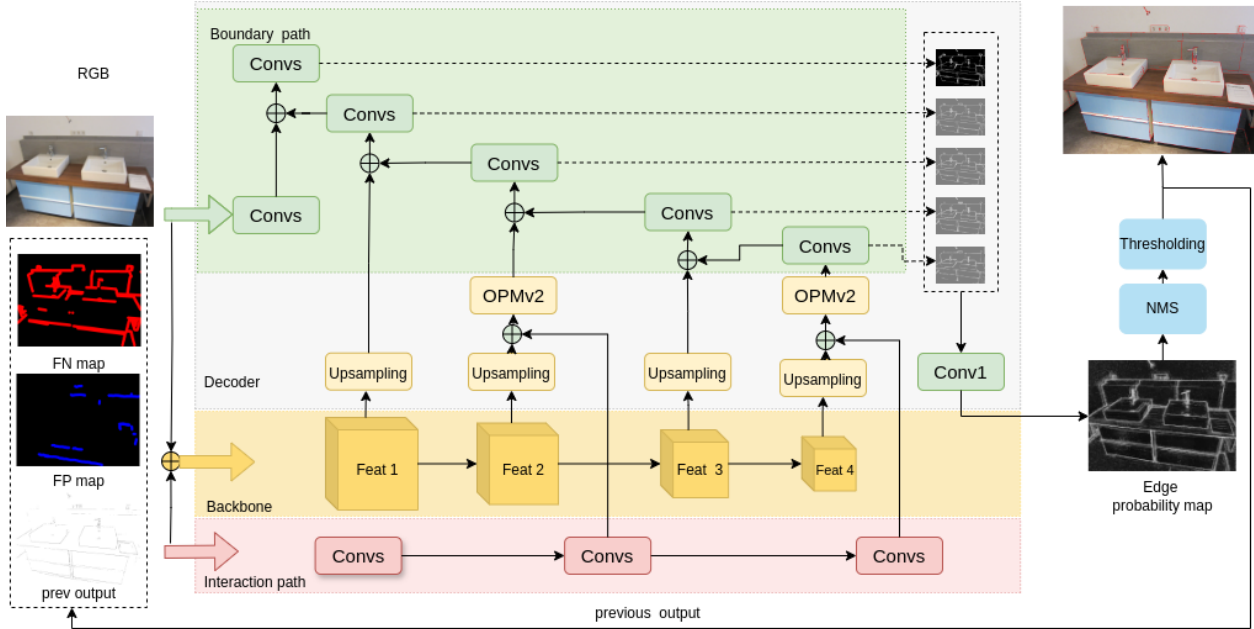


Figure 2. The Overall Pipeline of DNMSI

respect to the definition of *thresholding* and the models of the involved individual deep-learning components.

Interaction Mechanism For simplicity and efficiency, we mainly consider the case where one initial estimation result is provided to the user, and then all interaction scribbles are given for estimation in a single iteration.

Training & Testing The training process consists of two stages. In the first stage, we acquire the set of FN boundary segments by randomly selecting from the GT boundaries and obtain the set of FP boundary segments from pieces in Canny-detected edges absent in the GT boundaries. Then *scribble simulation* presented below is applied to them so as to obtain the FN-scribbles and the FP-scribbles. The network is trained using the training set of RGB images, along with the corresponding FN-FP maps and an all-zero map as the initial previous output. In the second stage, the training data are divided into a sequence of small batches and the training process is carried out progressively batch by batch. For each batch of images: (i) The FN-FP map and the previous network output are initialized as all-zero maps to get the output using the current configuration of the model. This output and the GTs are compared to get the set of FN and FP boundary segments. They are then sorted by length and the first ones are selected to get the FN-scribbles and the FP-scribbles via *scribble simulation*, which are then used to get the FN-FP map; (ii) The input images, together with the outputs and the FN-FP maps obtained in (i), are used to train and update the model’s configuration.

Similar to interactive segmentation, machine-simulated interaction is mainly used in the testing process, where the

prediction on an image consists of two steps: (i) It is similar to the training process based on a batch of images. (ii) The input images, together with the outputs and the FN-FP maps obtained in (i), are used to get the final output. In the case of human interaction, the FN-scribbles and the FP-scribbles in (i) are provided by the user.

Scribble Simulation We simulate the FN/FP-scribbles and get the FN-FP map, by (i) introducing perturbations in both length and location to the set of FN/FP boundary segments and then (ii) using a disk kernel to dilate the resulting point sets. The length perturbation is done by randomly lengthening/shortening the boundaries. And the position perturbation is applied after length perturbation, wherein each pixel point in the boundary segments receives an individual random perturbation of maximal extent. Regarding (ii), it can be simply implemented by applying the disk encoding (*i.e.*, [56]) to the resulting point sets.

3.3. Synthetic Benchmark Generation

We introduce *Mesh2OB* for synthetic benchmark generation, of which the overall idea is: given the 3D scene data represented by meshes and the corresponding camera model, (i) Blender is employed to generate RGBA images, along with associated data such as depth maps, normal maps, and other related information; (ii) (for the purpose of precision), we developed a Python code to fully explore the geometric information of the 3D meshes to get the GT occlusion boundaries for the image taken under the given camera, based on the definition given in [62]. More details, the pseudo-code, and its limitations are stated in the SM.

4. Experimental Results

In this section, we sequentially present the experimental setup, the qualitative and quantitative results, and the ablation studies. More experiments and ablation studies can be found in the supplementary materials.



Figure 3. **Comparison of the Quality of OB Generation between *Mesh2OB* and the method of [48].** *Mesh2OB*: the union of those boundaries in white & red; [48]: those boundaries in white.

4.1. Experimental Setup

Datasets In the experiments described in Section 4, unless otherwise specified, the proposed *DNMMSI* was trained using the synthetic benchmark *OB-FUTURE*. The testing was conducted based on *OB-LabName* and also the previous OB benchmarks, the exact dataset(s) will be stated in the presentation of each experiment. Below is a brief introduction of *OB-FUTURE* and *OB-LabName*:

- ***OB-FUTURE*** is built by applying the generation method presented in Section 3.3 on the *3D-FUTURE* dataset [13]. Details of *OB-FUTURE* are presented in Table 1. From the data, we selected 12,632 examples for the training set and 190 for the testing set, ensuring no overlap of furniture between the two sets⁶. Fig. 3 shows two samples of *OB-FUTURE*, together with the advantages over the method of [48]: the complete object occlusion contours and more accurate self-occlusion boundaries.
- ***OB-LabName*** is composed of two subsets *OB-DIODE* and *OB-EntitySeg*, which are constructed by labeling 50 and 70 images from a standard dataset for monocular depth estimation named *Diode Dense Indoor/Outdoor DEpth (DIODE)* [60] and a recent entity segmentation dataset collection *EntitySeg* [38],

⁶Further details can be found in the supplementary materials.

respectively, using ByLabel [47], an edge-level image annotation tool. The image resolution for *OB-DIODE* is (1024, 768), and for *OB-EntitySeg*, it ranges from (747, 1333) to (750, 1333). Examples can be found in Fig. 4.

In Table 1, we present general information about six previous OB datasets and compare the characteristics of their GTs. Our datasets feature not only high-resolution scenes, but also high-quality GT OB annotations across four aspects: full-image OB annotation, complete object occlusion contours, consideration of self-occlusion boundaries, and inclusion of non-closed cases.

Implementation Details Our network is implemented in *PyTorch*. The main backbone is *Swinformer architecture* [37], unless explicitly stated otherwise. The disk’s radius for performing the scribble simulation is 12. The first training stage is conducted over 4 epochs and the second stage is started from epoch 5. During the training process, the maximum allowable number of candidate FN/FP boundary segments is 5. For the other training hyperparameters, we keep the same as those used in *OPNet* [12]. In the testing, unless explicitly stated otherwise, machine-simulated interaction is used. All the FN and FP boundary segments of which the length is larger than 30 are taken to generate FN-scribbles and the FP-scribbles for general experimental evaluations, while in ablation comparison, the maximal numbers of FNs and FPs are limited to 12. All the compared IS models and our network are trained in the same environments with the same experimental setting.

Regarding the *thresholding* process in Fig. 2 on the probability map $P(\cdot)$ produced by NMS, (i) The final output $O(\cdot)$ is a binary map obtained by: $O(x, y) = 1$, if $Pr(x, y) \geq T$ or 0, if $I(x, y) < T$. During the training process, T is set to 0.7, and in the testing phase, T is automatically determined by the MATLAB evaluation code, consistent with the approach taken in closely related works [12, 39, 48, 64, 65]. (ii) To obtain the *previous output*, since it does not need to be a binary map, it can be derived in the same way as the final output (referred to as the *binary version*) or by simply setting values below the threshold to 0 (referred to as the *non-binary version*).

Different versions of *DNMMSI* can be implemented by using different alternatives for some components. Here, we present the results of two particular versions: (i) *v1* (the default version) uses the *PyTorch* upsampling layer with the *previous output* as the *non-binary version*; (ii) *v2* employs pixel shuffle [55] for upsampling the backbone feature map, with the *previous output* as the *binary version*.

Evaluation Metrics *Precision & Recall (PR)* are calculated using the same protocol as those closely related works [12, 39, 48, 64, 65]. Furthermore, the following 3 standard metrics are calculated from PR: (i) *Fixed contour threshold (ODS)*, which is the F-measure with the best fixed occlusion boundary probability threshold over the all datasets;



Figure 4. Qualitative Results on *OB-LabName*

(ii) *Best threshold of image (OIS)*, which is F-measure with the best occlusion boundary probability threshold for each image; (iii) *Average precision (AP)*, which is the average precision over all occlusion probability thresholds.

Regarding the level of user effort required to refine the estimation results, due to the difference from interactive segmentation as stated in Section 3.3, *Number of Clicks (NoC)* required on average to reach a certain IOU value (e.g., 85, 90, 95%) for a single object is not pertinent. To this end, *avgFN* and *avgFP* are employed, defined as the averages of the ratios between the numbers of pixels occupied by FN or FP boundary segments used for generating scribbles and the total number of GT or non-GT pixel points, respectively. They, to some extent, indicate the model’s capacity to detect occlusions without human interactions and the level of user effort needed in the annotation process.

4.2. Qualitative & Quantitative Results

Fig. 4 shows the qualitative results of *DNMMSI* on 6 representative images (first three rows for *OB-DIODE*, last three for *OB-EntitySeg*). The overall performance is promising, with interaction significantly improving prediction quality.

Considering the fact that there is no previous work on the exact problem, we have devised 7 alternative methods by incorporating the deep networks of the interactive segmentation methods introduced by [6, 7, 32–34, 36, 56] into the pipeline of *DNMMSI*. Besides, we have evaluated the performance of a fully automatic method *OPNet*, which is the SOTA work of the occlusion relation reasoning. Table 2 presents the quantitative results achieved by them as well as by different versions of *DNMMSI*. Below are some key observations: (i) *DNMMSI* achieves the highest ODS, OIS, and AP metrics on both *OB-DIODE* and

Table 2. **Quantitative Results & Comparison.** The first row/block shows the results of the fully-automatic method OPNet. Blocks 2-5 compare *DNMMSI* with alternative methods, indicated by their names. The last block presents additional results of *DNMMSI*. *w/t prev* indicates that the prev output is not employed in the model. Optimal results in each block or overall are highlighted with underlined or **bold** formatting. Metric values in **red/blue** indicate that our method outperforms/underperforms the previous method with the same backbone. These conventions are used throughout the paper and the supplementary materials (SM), unless explicitly stated otherwise.

Method	Backbone	<i>OB-DIODE</i>					<i>OB-EntitySeg</i>				
		ODS	OIS	AP	avgFN (10^{-2})	avgFP (10^{-4})	ODS	OIS	AP	avgFN (10^{-2})	avgFP (10^{-3})
OPNet [12]	ResNet50	72.8	74.0	61.8	-	-	50.7	57.7	36.8	-	-
RITM [56]	HRNet18s	75.0	78.3	75.2	10.1	15.6	42.7	55.8	25.3	11.3	23.1
RITM [56]	HRNet18	75.0	78.0	76.0	10.0	28.1	32.8	35.1	13.7	10.4	41.5
RITM [56]	HRNet32	73.6	78.3	74.5	6.0	29.5	33.2	34.9	15.0	9.5	30.6
Ours	HRNet18s	<u>70.7</u>	<u>76.8</u>	<u>70.4</u>	45.1	5.1	<u>64.6</u>	<u>66.2</u>	<u>61.5</u>	21.5	28.2
Ours	HRNet18	<u>79.6</u>	<u>83.2</u>	<u>82.8</u>	35.8	7.7	<u>73.8</u>	<u>75.3</u>	<u>77.5</u>	21.4	17.5
Ours	HRNet32	<u>76.6</u>	<u>82.5</u>	<u>82.9</u>	35.9	6.0	<u>67.8</u>	<u>71.2</u>	<u>70.7</u>	17.7	10.5
CDNet [6]	ResNet34	67.6	71.2	65.6	8.8	69.6	43.2	50.7	35.3	8.8	7.0
TOS-Net [32]	ResNet50	74.8	81.8	60.4	10.6	58.3	69.0	70.9	54.9	15.6	8.2
FCA-Net [34]	ResNet101	77.1	82.6	81.9	24.4	14.9	71.8	75.2	73.7	13.0	23.6
Ours	ResNet34	<u>83.0</u>	<u>85.7</u>	<u>89.1</u>	26.8	6.0	<u>67.5</u>	<u>72.2</u>	<u>63.6</u>	10.7	16.7
Ours	ResNet50	<u>76.7</u>	<u>81.5</u>	<u>82.7</u>	67.2	0.4	<u>73.3</u>	<u>74.6</u>	<u>75.8</u>	33.6	17.7
Ours	ResNet101	<u>78.4</u>	<u>83.0</u>	<u>82.7</u>	63.8	0.3	<u>72.7</u>	<u>76.6</u>	<u>73.0</u>	35.7	10.0
FocalClick [7]	SegF-B0	73.9	79.0	76.9	9.5	13.0	63.3	69.0	68.6	6.5	32.9
FocalClick [7]	SegF-B3	<u>78.8</u>	81.9	<u>82.2</u>	11.4	9.7	57.3	63.0	46.0	8.6	16.5
Ours	SegF-B0	<u>74.0</u>	<u>80.2</u>	<u>79.9</u>	50.0	4.8	<u>66.6</u>	<u>69.2</u>	<u>71.2</u>	26.3	8.4
Ours	SegF-B3	<u>77.1</u>	<u>82.2</u>	<u>77.8</u>	48.1	6.2	<u>76.1</u>	<u>78.0</u>	<u>77.3</u>	26.9	7.6
AdaptiveClick [33]	ViT-B	75.8	79.8	79.0	3.2	21.5	66.2	69.7	64.2	4.9	12.5
SimpleClick [36]	ViT-B	73.6	78.5	78.2	3.2	24.0	69.5	71.4	70.0	5.3	97.1
SimpleClick [36]	ViT-L	72.1	76.6	76.8	6.3	22.3	63.4	66.1	62.1	5.4	11.6
Ours	ViT-B	<u>80.9</u>	<u>85.9</u>	<u>87.4</u>	23.3	7.3	<u>80.8</u>	<u>82.4</u>	<u>87.1</u>	9.1	5.6
Ours	ViT-L	<u>81.0</u>	<u>85.1</u>	<u>87.6</u>	23.6	14.2	<u>80.0</u>	<u>81.3</u>	<u>85.7</u>	9.4	8.1
Ours v1	Swin-S	84.2	87.0	89.4	20.0	6.1	81.2	82.1	86.4	20.0	46.8
Ours v1	Swin-B	85.5	87.9	90.0	18.0	8.3	81.3	82.5	86.4	17.4	4.2
Ours v2	Swin-L	86.9	88.2	91.2	35.2	4.0	80.5	81.9	84.3	24.2	5.7
Ours v1	Swin-L	84.8	87.0	89.7	19.2	5.7	79.1	80.2	82.1	13.0	11.3
Ours v1 w/t prev	Swin-L	86.8	88.1	91.7	14.0	11.8	77.0	79.2	80.8	13.5	23.5

OB-EntitySeg; (ii) *DNMMSI* achieves significantly superior metrics (e.g., ODS improvement: 14.1, OIS improvement: 14.2, and AP improvement: 29.4 on *OB-DIODE*) compared to OPNet, highlighting the efficacy of interaction in occlusion boundary estimation; (iii) Overall, *DNMMSI*, utilizing the same backbone, outperforms its competitors in ODS/OIS/AP; (iv) The use of Swinformer in *DNMMSI* performs the best among all the tested backbones; (v) *DNMMSI* initially exhibited fewer false positive (FP) edges but more false negatives (FN) than the competitors. However, the integration of scribble-based interaction significantly improved *DNMMSI*'s performance, surpassing that of the competitors, demonstrating the reasonableness of our design of the deep network in the pipeline. Finally, it is worth mentioning that the metrics of the avgFN/avgFP are shown in Table 2 for indicating the annotator's involvement in refining the prediction. They are not the real False positive/negative rate, since only the pixels in the scribbles are taken into account, of which the corresponding selected FN/FP-boundary segments have lengths greater than 30.

Moreover, we have evaluated the performance of both our *DNMMSI* and OPNet using the previous benchmarks, as well as *OB-FUTURE*. The quantitative results are presented in Table 3, illustrating the following: (i) the improvement achieved by *DNMMSI* over the SOTA fully-automatic method, which underscores its effectiveness in leveraging human interaction; (ii) the promising results when *DNMMSI* is trained and tested on real data (in contrast to the

experiments presented in Table 2); and (iii) the effectiveness of *DNMMSI* extends beyond the estimation of the full OB map defined in [62]. More comparisons with interactive competitors and other details are provided in the SM.

Table 3. **Comparisons between *DNMMSI* and the Fully-Automatic OPNet on more Datasets.**

Method	Dataset	ODS	OIS	AP
OPNet	<i>PIOD</i>	78.6	79.6	79.5
<i>DNMMSI</i>		<u>88.7</u>	<u>89.5</u>	<u>91.4</u>
OPNet	<i>NYUv2-OC++</i>	65.1	66.2	55.4
<i>DNMMSI</i>		<u>78.5</u>	<u>79.4</u>	<u>82.8</u>
OPNet	<i>BSDS ownership</i>	67.2	70.3	66.8
<i>DNMMSI</i>		<u>78.3</u>	<u>79.2</u>	<u>79.6</u>
OPNet	<i>OB-FUTURE</i>	88.8	89.5	85.9
<i>DNMMSI</i>		<u>89.9</u>	<u>90.8</u>	<u>88.2</u>

Lastly, we measured the annotation time using 20 samples from *OB-DIODE* and *OB-EntitySeg*, as shown in Table 4. Manual annotation takes 6 ~ 8 times longer and requires significantly more meticulous effort compared to using *DNMMSI*. These findings underscore the significance and potential of studying interactive OB estimation.

Table 4. **Annotation Time of *DNMMSI* on *OB-LabName*.**

Dataset	Time cost (mins)	ODS	OIS	AP
<i>OB-DIODE</i>	5±1	88.8	89.2	90.7
<i>OB-EntitySeg</i>	6±1.5	84.8	86.1	86.8

4.3. Ablation Study

We conducted a series of ablation studies to better understand *DNMMSI*. In all related experiments, the models are trained by *OB-FUTURE* and evaluated on *OB-DIODE*.

Firstly, we conducted experiments to assess how Swin-former’s performance varies with different disk kernel radii for generating FN/FP scribbles. The results in Table 5 indicate that the performance of *DNMMSI* does not consistently improve with a smaller radius.

Table 5. Results on Different Disk Kernel Radii.

Radius	ODS	OIS	AP
3	77.9	84.4	73.5
5	79.6	82.5	83.0
7	80.5	83.8	82.4
10	79.2	81.9	81.5
12	81.6	83.6	83.8
14	79.0	81.5	81.9
16	80.5	82.6	82.7
18	78.0	81.0	79.7
20	76.5	80.9	78.9

Secondly, we examined *DNMMSI* with different Starts of the Second Training Stage (SSTS). As mentioned in Section 3.2, we set the training process with two stages, and $SSIT = N$ means that the first training stage is conducted over $N - 1$ epochs). The obtained results shown in Table 6 indicate that the optimal performance is achieved when the first stage is done by 4 epochs, which also substantiates the rationale behind conducting two-stage learning.

Table 6. Performance Variation with Different SSTS.

SSTS	ODS	OIS	AP
1	31.0	47.7	23.0
2	70.0	75.5	70.0
3	78.8	81.6	81.8
4	80.0	82.3	83.3
5	82.4	84.1	84.7
6	82.2	84.1	85.2
7	81.3	83.3	83.6

Thirdly, we evaluated the impact of the threshold value T used in the thresholding process to obtain the *previous output*, on the final performance of *DNMMSI*. The results, presented in Table 7, indicate that the best performance is achieved when T is set around 0.7.

Table 7. Results obtained Using Different Threshold Values.

OBPT	ODS	OIS	AP
0.51	80.8	83.8	83.3
0.60	82.0	83.9	84.4
0.70	82.4	84.1	84.7
0.75	80.8	83.8	83.3
0.80	78.9	81.2	78.3
0.85	78.1	80.7	77.0
0.90	78.2	80.6	76.7

Fourthly, we quantitatively evaluated the performance obtained by: (i) eliminating the previous network output in the model input, and (ii) using the progressive interactive estimation, wherein the FN/FP-scribbles are generated iteratively instead of all at once within a single iteration. At

each iteration, at most one FN-scribble and one FP-scribble are generated using the same selection principle as that of *DNMMSI*. The metrics in Table 8 demonstrate the benefit of the choices in these two aspects within *DNMMSI*. Furthermore, the running time for one iteration of the progressive interactive estimation is approximately the same as *DNMMSI*, and thus requires much more time for inference.

Table 8. Results obtained by *DNMMSI* and two Variations.

Pre Output	Progressive	ODS	OIS	AP
+	-	82.4	84.1	84.7
-	-	81.5	83.9	86.1
+	+	74.7	83.0	79.6

Finally, we show in Table 9 the results achieved by three key variations of the aforementioned presented design of *DNMMSI* obtained by eliminating the interaction path (used for additionally processing the FN-FP map and the previous network output and aggregating the obtained features with the backbone features before passing to OPMv2 modules), the upsampling layer, and/or the OPMv2 modules. These quantitative results validate the choice of the final design for *DNMMSI*.

Table 9. Results on Different Network Architecture Variations.

Interaction path	upsampling	OPMv2	ODS	OIS	AP
-	+	-	74.6	82.6	77.5
+	-	-	44.3	59.1	40.7
+	+	-	82.4	84.1	84.7
+	+	+	82.4	84.2	86.8

5. Conclusion and Future Work

In this paper, we introduced *DNMMSI*, a deep-network-based method for interactive occlusion boundary (OB) estimation; *Mesh2OB*, a tool for generating 2D images with OB ground truths from 3D scene mesh data; and *OB-LabName*, a real benchmark for robust evaluation in OB-related research. Experimental results demonstrate that: (i) our method delivers promising performance by leveraging synthetic data without domain adaptation, with the potential for even better results under optimal conditions; (ii) interactive OB estimation is highly effective for labeling OB ground truths in monocular images.

Aside from the potential for improvement, two main limitations of this work are: (i) *DNMMSI* would struggle with images where the OBs are so densely packed that the space between them becomes too narrow relative to the width of the scribbles; (ii) the experimental validation was conducted only on indoor images, due to the lack of sufficient 3D mesh data for outdoor scenes. Based on the current overall framework, two promising future directions are: (i) studying how to further enhance performance; and (ii) investigating effective approaches to address the aforementioned limitations.

References

- [1] Eirikur Agustsson, Jasper RR Uijlings, and Vittorio Ferrari. Interactive full image segmentation by considering all regions jointly. In *Proceedings of the IEEE/CVF Conference on Computer Vision and Pattern Recognition (CVPR)*, pages 11622–11631, 2019. [3](#)
- [2] Mykhaylo Andriluka, Stefano Pellegrini, Stefan Popov, and Vittorio Ferrari. Efficient full image interactive segmentation by leveraging within-image appearance similarity. *arXiv preprint arXiv:2007.08173*, 2020. [3](#)
- [3] Nicholas Apostoloff and Andrew Fitzgibbon. Learning spatiotemporal t-junctions for occlusion detection. In *IEEE Computer Society Conference on Computer Vision and Pattern Recognition (CVPR)*, pages 553–559, 2005. [1](#), [2](#)
- [4] Michael J Black. Combining intensity and motion for incremental segmentation and tracking over long image sequences. In *Proceedings of the European Conference on Computer Vision (ECCV)*, pages 485–493, 1992. [1](#)
- [5] Umberto Castellani, Salvatore Livatino, and Robert B Fisher. Improving environment modelling by edge occlusion surface completion. In *Proceedings. First International Symposium on 3D Data Processing Visualization and Transmission*, pages 672–675, 2002. [1](#)
- [6] Xi Chen, Zhiyan Zhao, Feiwu Yu, Yilei Zhang, and Manni Duan. Conditional diffusion for interactive segmentation. In *Proceedings of the IEEE/CVF International Conference on Computer Vision (ICCV)*, pages 7345–7354, 2021. [2](#), [6](#), [7](#)
- [7] Xi Chen, Zhiyan Zhao, Yilei Zhang, Manni Duan, Donglian Qi, and Hengshuang Zhao. Focalclick: towards practical interactive image segmentation. In *Proceedings of the IEEE/CVF Conference on Computer Vision and Pattern Recognition (CVPR)*, pages 1300–1309, 2022. [2](#), [6](#), [7](#)
- [8] Xi Chen, Yau Shing Jonathan Cheung, Ser-Nam Lim, and Hengshuang Zhao. Scribbleseg: Scribble-based interactive image segmentation. *arXiv preprint arXiv:2303.11320*, 2023. [2](#), [3](#)
- [9] Fei Du, Jianlong Yuan, Zhibin Wang, and Fan Wang. Efficient mask correction for click-based interactive image segmentation. In *Proceedings of the IEEE/CVF Conference on Computer Vision and Pattern Recognition (CVPR)*, pages 22773–22782, 2023. [2](#)
- [10] Camille Dupont, Yanis Ouakrim, and Quoc Cuong Pham. Ucp-net: unstructured contour points for instance segmentation. In *IEEE International Conference on Systems, Man, and Cybernetics (SMC)*, pages 3373–3379. IEEE, 2021. [3](#)
- [11] Doron Feldman and Daphna Weinshall. Motion segmentation and depth ordering using an occlusion detector. *IEEE Transactions on Pattern Analysis and Machine Intelligence (TPAMI)*, 30(7):1171–1185, 2008. [2](#)
- [12] Panhe Feng, Qi She, Lei Zhu, Jiabin Li, Lin Zhang, Zijian Feng, Changhu Wang, Chunpeng Li, Xuejing Kang, and Anlong Ming. Mt-ori: Multi-task occlusion relationship learning. In *Proceedings of the IEEE/CVF International Conference on Computer Vision (ICCV)*, pages 9364–9373, 2021. [1](#), [2](#), [3](#), [5](#), [7](#)
- [13] Huan Fu, Rongfei Jia, Lin Gao, Mingming Gong, Binqiang Zhao, Steve Maybank, and Dacheng Tao. 3d-future: 3d future shape with texture. *International Journal of Computer Vision (IJCV)*, 129:3313–3337, 2021. [2](#), [5](#)
- [14] Praful Hambarde, Gourav Wadhwa, Santosh Kumar Vipparthi, Subrahmanyam Murala, and Abhinav Dhall. Occlusion boundary prediction and transformer based depth-map refinement from single image. *ACM Transactions on Multimedia Computing, Communications and Applications*, 2024. [1](#), [2](#)
- [15] Nazim Haouchine, Jeremie Dequidt, Marie-Odile Berger, and Stephane Cotin. Monocular 3d reconstruction and augmentation of elastic surfaces with self-occlusion handling. *IEEE Transactions on Visualization and Computer Graphics*, 21(12):1363–1376, 2015. [1](#)
- [16] Xuming He and Alan Yuille. Occlusion boundary detection using pseudo-depth. In *Proceedings of the European Conference on Computer Vision (ECCV)*, pages 539–552, 2010. [1](#), [2](#)
- [17] Derek Hoiem, Andrew N Stein, Alexei A Efros, and Martial Hebert. Recovering occlusion boundaries from a single image. In *Proceedings of the IEEE/CVF International Conference on Computer Vision (ICCV)*, pages 1–8, 2007. [1](#), [2](#)
- [18] You Huang, Hao Yang, Ke Sun, Shengchuan Zhang, Lijuan Cao, Guannan Jiang, and Rongrong Ji. Interformer: Real-time interactive image segmentation. In *Proceedings of the IEEE/CVF International Conference on Computer Vision (ICCV)*, pages 22301–22311, 2023. [2](#)
- [19] Natan Jacobson, Yoav Freund, and Truong Q Nguyen. An online learning approach to occlusion boundary detection. *IEEE Transactions on Image Processing (TIP)*, 21(1):252–261, 2011. [2](#)
- [20] Won-Dong Jang and Chang-Su Kim. Interactive image segmentation via backpropagating refinement scheme. In *Proceedings of the IEEE/CVF Conference on Computer Vision and Pattern Recognition (CVPR)*, pages 5297–5306, 2019. [2](#)
- [21] Zhaoyin Jia, Andrew Gallagher, Yao-Jen Chang, and Tsuhan Chen. A learning-based framework for depth ordering. In *Proceedings of the IEEE/CVF Conference on Computer Vision and Pattern Recognition (CVPR)*, pages 294–301, 2012. [1](#)
- [22] Kevin Karsch, Zicheng Liao, Jason Rock, Jonathan T Barron, and Derek Hoiem. Boundary cues for 3d object shape recovery. In *Proceedings of the IEEE Conference on Computer Vision and Pattern Recognition (CVPR)*, pages 2163–2170, 2013. [1](#)
- [23] Michael Keller, Reinhard Knothe, and Thomas Vetter. 3d reconstruction of human faces from occluding contours. In *Computer Vision/Computer Graphics Collaboration Techniques*, pages 261–273, 2007. [1](#)
- [24] Rawal Khirodkar, Shashank Tripathi, and Kris Kitani. Occluded human mesh recovery. In *Proceedings of the IEEE/CVF Conference on Computer Vision and Pattern Recognition (CVPR)*, pages 1715–1725, 2022. [1](#)
- [25] Tobias Koch, Lukas Liebel, Friedrich Fraundorfer, and Marco Korner. Evaluation of cnn-based single-image depth estimation methods. In *Proceedings of the European Conference on Computer Vision Workshops (ECCVW)*, pages 0–0, 2018. [2](#)

- [26] Hoang Le, Long Mai, Brian Price, Scott Cohen, Hailin Jin, and Feng Liu. Interactive boundary prediction for object selection. In *Proceedings of the European Conference on Computer Vision (ECCV)*, pages 18–33, 2018. 3
- [27] Chunggi Lee, Seonwook Park, Heon Song, Jeongun Ryu, Sanghoon Kim, Haejoon Kim, Sérgio Pereira, and Donggeun Yoo. Interactive multi-class tiny-object detection. In *Proceedings of the IEEE/CVF Conference on Computer Vision and Pattern Recognition (CVPR)*, pages 14136–14145, 2022. 2
- [28] Jianwei Li, Wei Gao, and Yihong Wu. High-quality 3d reconstruction with depth super-resolution and completion. *IEEE Access*, 7:19370–19381, 2019. 1
- [29] Ruizhe Li and Xin Chen. An efficient interactive multi-label segmentation tool for 2d and 3d medical images using fully connected conditional random field. *Computer Methods and Programs in Biomedicine*, 213:106534, 2022. 2
- [30] Wenbin Li, Sajad Saeedi, John McCormac, Ronald Clark, Dimos Tzoumanikas, Qing Ye, Yuzhong Huang, Rui Tang, and Stefan Leutenegger. Interiornet: Mega-scale multi-sensor photo-realistic indoor scenes dataset. *arXiv preprint arXiv:1809.00716*, 2018. 2
- [31] Zongcheng Li, Xiaoxiao Long, Yusen Wang, Tuo Cao, Wenping Wang, Fei Luo, and Chunxia Xiao. Neto: neural reconstruction of transparent objects with self-occlusion aware refraction-tracing. In *Proceedings of the IEEE/CVF International Conference on Computer Vision (ICCV)*, pages 18547–18557, 2023. 1
- [32] Jun Hao Liew, Scott Cohen, Brian Price, Long Mai, and Jia-shi Feng. Deep interactive thin object selection. In *Proceedings of the IEEE/CVF Winter Conference on Applications of Computer Vision (WACV)*, pages 305–314, 2021. 2, 3, 6, 7
- [33] Jiacheng Lin, Jiajun Chen, Kailun Yang, Alina Roitberg, Siyu Li, Zhiyong Li, and Shutao Li. Adaptiveclick: Clicks-aware transformer with adaptive focal loss for interactive image segmentation. *arXiv preprint arXiv:2305.04276*, 2023. 7
- [34] Zheng Lin, Zhao Zhang, Lin-Zhuo Chen, Ming-Ming Cheng, and Shao-Ping Lu. Interactive image segmentation with first click attention. In *Proceedings of the IEEE/CVF Conference on Computer Vision and Pattern Recognition (CVPR)*, pages 13339–13348, 2020. 2, 6, 7
- [35] Zheng Lin, Zheng-Peng Duan, Zhao Zhang, Chun-Le Guo, and Ming-Ming Cheng. Focuscut: Diving into a focus view in interactive segmentation. In *Proceedings of the IEEE/CVF Conference on Computer Vision and Pattern Recognition (CVPR)*, pages 2637–2646, 2022.
- [36] Qin Liu, Zhenlin Xu, Gedas Bertasius, and Marc Niethammer. Simpleclick: Interactive image segmentation with simple vision transformers. In *Proceedings of the IEEE/CVF International Conference on Computer Vision (ICCV)*, pages 22290–22300, 2023. 2, 6, 7
- [37] Ze Liu, Yutong Lin, Yue Cao, Han Hu, Yixuan Wei, Zheng Zhang, Stephen Lin, and Baining Guo. Swin transformer: Hierarchical vision transformer using shifted windows. In *Proceedings of the IEEE/CVF International Conference on Computer Vision (ICCV)*, pages 10012–10022, 2021. 5
- [38] Qi Lu, Jason Kuen, Shen Tiancheng, Gu Jiuxiang, Guo Weidong, Jia Jiaya, Lin Zhe, and Yang Ming-Hsuan. High-quality entity segmentation. In *Proceedings of the IEEE/CVF International Conference on Computer Vision (ICCV)*, pages 4047–4056, 2023. 2, 5
- [39] Rui Lu, Feng Xue, Menghan Zhou, Anlong Ming, and Yu Zhou. Occlusion-shared and feature-separated network for occlusion relationship reasoning. In *Proceedings of the IEEE/CVF International Conference on Computer Vision (ICCV)*, pages 10343–10352, 2019. 2, 5
- [40] Xiangde Luo, Guotai Wang, Tao Song, Jingyang Zhang, Michael Aertsen, Jan Deprest, Sebastien Ourselin, Tom Vercauteren, and Shaoting Zhang. Mideepseg: Minimally interactive segmentation of unseen objects from medical images using deep learning. *Medical Image Analysis*, 72:102102, 2021. 2
- [41] Soumajit Majumder, Abhinav Rai, Ansh Khurana, and Angela Yao. Two-in-one refinement for interactive segmentation. In *British Machine Vision Conference (BMVC)*, page 2, 2020. 3
- [42] Kevis-Kokitsi Maninis, Sergi Caelles, Jordi Pont-Tuset, and Luc Van Gool. Deep extreme cut: From extreme points to object segmentation. In *Proceedings of the IEEE Conference on Computer Vision and Pattern Recognition (CVPR)*, pages 616–625, 2018. 3
- [43] Anlong Ming, Tianfu Wu, Jianxiang Ma, Fang Sun, and Yu Zhou. Monocular depth-ordering reasoning with occlusion edge detection and couple layers inference. *IEEE Intelligent Systems*, 31(2):54–65, 2015. 1
- [44] Claudia Nieuwenhuis and Daniel Cremers. Spatially varying color distributions for interactive multilabel segmentation. *IEEE Transactions on Pattern Analysis and Machine Intelligence (TPAMI)*, 35(5):1234–1247, 2012. 3
- [45] Claudia Nieuwenhuis, Simon Hawe, Martin Kleinsteuber, and Daniel Cremers. Co-sparse textural similarity for interactive segmentation. In *Proceedings of the European Conference on Computer Vision (ECCV)*, pages 285–301, 2014. 3
- [46] Polina Popenova, Danil Galeev, Anna Vorontsova, and Anton Konushin. Contour-based interactive segmentation. In *Proceedings of the Thirty-Second International Joint Conference on Artificial Intelligence*, pages 1322–1330, 2023. 3
- [47] Xuebin Qin, Shida He, Zichen Zhang, Masood Dehghan, and Martin Jagersand. Bylabel: A boundary based semi-automatic image annotation tool. In *Proceedings of the IEEE/CVF Winter Conference on Applications of Computer Vision (WACV)*, pages 1804–1813, 2018. 5
- [48] Xuchong Qiu, Yang Xiao, Chaohui Wang, and Renaud Marlet. Pixel-pair occlusion relationship map (p2orm): formulation, inference and application. In *Proceedings of the European Conference on Computer Vision (ECCV)*, pages 690–708, 2020. 1, 2, 3, 5
- [49] Michael Ramamonjisoa and Vincent Lepetit. Sharpnet: Fast and accurate recovery of occluding contours in monocular depth estimation. In *Proceedings of the IEEE/CVF International Conference on Computer Vision Workshops (ICCVW)*, pages 0–0, 2019. 1

- [50] Michael Ramamonjisoa, Yuming Du, and Vincent Lepetit. Predicting sharp and accurate occlusion boundaries in monocular depth estimation using displacement fields. In *Proceedings of the IEEE/CVF Conference on Computer Vision and Pattern Recognition (CVPR)*, pages 14648–14657, 2020. 2, 3
- [51] Ramesh Raskar, Kar-Han Tan, Rogerio Feris, Jingyi Yu, and Matthew Turk. Non-photorealistic camera: depth edge detection and stylized rendering using multi-flash imaging. *ACM Transactions on Graphics (TOG)*, 23(3):679–688, 2004.
- [52] Xiaofeng Ren, Charless C Fowlkes, and Jitendra Malik. Figure/ground assignment in natural images. In *Proceedings of the European Conference on Computer Vision (ECCV)*, pages 614–627, 2006. 2, 3
- [53] Jakob Santner, Thomas Pock, and Horst Bischof. Interactive multi-label segmentation. In *Asian Conference on Computer Vision (ACCV)*, pages 397–410, 2011. 3
- [54] Mehmet Emre Sargin, Luca Bertelli, Bangalore S Manjunath, and Kenneth Rose. Probabilistic occlusion boundary detection on spatio-temporal lattices. In *Proceedings of the IEEE/CVF International Conference on Computer Vision (ICCV)*, pages 560–567, 2009. 2
- [55] Wenzhe Shi, Jose Caballero, Ferenc Huszár, Johannes Totz, Andrew P Aitken, Rob Bishop, Daniel Rueckert, and Zehan Wang. Real-time single image and video super-resolution using an efficient sub-pixel convolutional neural network. In *Proceedings of the IEEE/CVF Conference on Computer Vision and Pattern Recognition (CVPR)*, pages 1874–1883, 2016. 5
- [56] Konstantin Sofiiuk, Ilya A Petrov, and Anton Konushin. Reviving iterative training with mask guidance for interactive segmentation. In *IEEE International Conference on Image Processing (ICIP)*, pages 3141–3145, 2022. 2, 4, 6, 7
- [57] Andrew N Stein and Martial Hebert. Occlusion boundaries from motion: Low-level detection and mid-level reasoning. *International Journal of Computer Vision (IJCV)*, 82:325–357, 2009. 2, 3
- [58] Patrik Sundberg, Thomas Brox, Michael Maire, Pablo Arbeláez, and Jitendra Malik. Occlusion boundary detection and figure/ground assignment from optical flow. In *IEEE Computer Society Conference on Computer Vision and Pattern Recognition (CVPR)*, pages 2233–2240, 2011. 1, 2
- [59] Ching Teo, Cornelia Fermuller, and Yiannis Aloimonos. Fast 2d border ownership assignment. In *Proceedings of the IEEE Conference on Computer Vision and Pattern Recognition (CVPR)*, pages 5117–5125, 2015. 2
- [60] Igor Vasiljevic, Nick Kolkin, Shanyi Zhang, Ruotian Luo, Haochen Wang, Falcon Z Dai, Andrea F Daniele, Mohammadreza Mostajabi, Steven Basart, Matthew R Walter, et al. Diode: A dense indoor and outdoor depth dataset. *arXiv preprint arXiv:1908.00463*, 2019. 2, 5
- [61] Vladimir Vezhnevets and Vadim Konouchine. Growcut: Interactive multi-label nd image segmentation by cellular automata. In *Graphicon*, pages 150–156, 2005. 3
- [62] Chaohui Wang, Huan Fu, Dacheng Tao, and Michael J Black. Occlusion boundary: A formal definition & its detection via deep exploration of context. *IEEE Transactions on Pattern Analysis and Machine Intelligence (TPAMI)*, 44(5):2641–2656, 2020. 1, 2, 4, 7
- [63] Guotai Wang, Wenqi Li, Maria A Zuluaga, Rosalind Pratt, Premal A Patel, Michael Aertsen, Tom Doel, Anna L David, Jan Depreest, Sébastien Ourselin, et al. Interactive medical image segmentation using deep learning with image-specific fine tuning. *IEEE Transactions on Medical Imaging*, 37(7):1562–1573, 2018. 2
- [64] Guoxia Wang, Xiaochuan Wang, Frederick WB Li, and Xiaohui Liang. Doobnet: Deep object occlusion boundary detection from an image. In *Asian Conference on Computer Vision (ACCV)*, pages 686–702, 2019. 1, 2, 5
- [65] Peng Wang and Alan Yuille. Doc: Deep occlusion estimation from a single image. In *Proceedings of the European Conference on Computer Vision (ECCV)*, pages 545–561, 2016. 1, 2, 3, 5
- [66] Ning Xu, Brian Price, Scott Cohen, Jimei Yang, and Thomas S Huang. Deep interactive object selection. In *Proceedings of the IEEE Conference on Computer Vision and Pattern Recognition (CVPR)*, pages 373–381, 2016. 2
- [67] ChangHee Yang, Kyeongbo Kong, SungJun Min, Dongyoon Wee, Ho-Deok Jang, Geonho Cha, and SukJu Kang. Sefd: learning to distill complex pose and occlusion. In *Proceedings of the IEEE/CVF International Conference on Computer Vision (ICCV)*, pages 14941–14952, 2023. 1
- [68] Shiyin Zhang, Jun Hao Liew, Yunchao Wei, Shikui Wei, and Yao Zhao. Interactive object segmentation with inside-outside guidance. In *Proceedings of the IEEE/CVF Conference on Computer Vision and Pattern Recognition (CVPR)*, pages 12234–12244, 2020. 2
- [69] Bolei Zhou, Hang Zhao, Xavier Puig, Sanja Fidler, Adela Barriuso, and Antonio Torralba. Scene parsing through ade20k dataset. In *Proceedings of the IEEE Conference on Computer Vision and Pattern Recognition (CVPR)*, pages 633–641, 2017. 1
- [70] Hao Zhu, Qing Wang, and Jingyi Yu. Occlusion-model guided antioclusion depth estimation in light field. *IEEE Journal of Selected Topics in Signal Processing*, 11(7):965–978, 2017. 1
- [71] Yan Zhu, Yuandong Tian, Dimitris Metaxas, and Piotr Dollár. Semantic amodal segmentation. In *Proceedings of the IEEE Conference on Computer Vision and Pattern Recognition (CVPR)*, pages 1464–1472, 2017. 1